International Journal of Mining Science and Technology 35 (2025) 1677–1693

Contents lists available at ScienceDirect

International Journal of Mining Science and Technology

journal homepage: www.elsevier.com/locate/ijmst

Electric ignition of sandstone fracturing in methane/air premixed gas in coal mines: Novel insights from ignition sources in a goaf

Wei Zhang [a,b], Deming Wang [a,b,*], Xuyao Qi [a,b], Chenguang Wang [a,b], Zhenlu Shao [a,b], Haihui Xin [a,b], Tengfei Chen [a,b], Zhenhai Hou [b,c]

[a] School of Safety Engineering, China University of Mining and Technology, Xuzhou 221116, China
[b] Key Laboratory of Gas and Fire Control for Coal Mines, China University of Mining and Technology, Ministry of Education, Xuzhou 221116, China
[c] College of Safety Science and Engineering, Henan Polytechnic University, Jiaozuo 454000, China

ARTICLE INFO

Article history:
Received 6 July 2025
Received in revised form 18 August 2025
Accepted 3 September 2025
Available online 25 October 2025

Keywords:
Gas explosions
Roof sandstone
Electric ignition
Luminous emission
Piezoelectric effect
Crack propagation

ABSTRACT

Gas explosions in coal mine goafs are associated with the roof rock fracturing. An experimental system was established to investigate the potential for electrical ignition induced by sandstone fracturing. The electrical responses, luminescent emissions, and ignition characteristics during tensile and compressive failure of sandstones were analyzed in methane/air premixed gas environments. Results indicate that the application of mechanical loading induces the emergence of electrical signals on rock surfaces and in the surrounding atmosphere. This phenomenon is attributed to the generation, accumulation, and subsequent release of free charges during the deformation and fracture within the sandstone. Compressive failure proved to be more conducive to free charge generation than tensile failure, owing to more crack connections. Furthermore, a precipitous increase in surface and external voltages was observed during complete fracturing, a consequence of electron emission from crack tips within the rock structure. Moreover, the ionization induces luminous emissions owing to the collision of energetic electrons released from gas molecules in methane/air mixtures. A strong positive correlation (R^2=0.9429) was identified between luminescence intensity and the magnitude of electrical discharge resulting from rock fracture. Notably, such discharge by rock fracturing can be capable of igniting the premixed gas, particularly when the quartz content exceeds 61%. Piezoelectric effects and crack propagation are crucial mechanisms in the causal chain of the charge generation, discharge, and ionization triggered by rock fractures. Based on the above laboratory results, electric ignition of the transient roof fracturing caused by stress mutations can serve as a new potential ignition source for gas explosions in the goaf. These results offer new insights into the prevention and control of gas explosions.

1. Introduction

Coal serves as a critical pillar for ensuring energy security and fostering the development of new energy sources [1,2]. However, gas explosions remain a significant threat to safe and efficient underground coal mining, particularly in China [3]. Between 2000 and 2024, gas explosions accounted for 61.2% of major accidents with more than 10 deaths in coal mines in China, resulting in 8589 deaths [4]. Recent severe gas explosion accidents in Colombia (March 14, 2023, 21 deaths), Kazakhstan (October 29, 2023, 45 deaths), and Iran (September 21, 2024, 51 deaths) underscore the continued prevalence of this hazard. Statistically, over a quarter of these gas explosions occur in goafs, where a porous confined space resulting from roof collapse provides favorable conditions for the premixing of methane and oxygen [5]. Despite the presence of these conditions, conventional ignition sources, such as electrical sparks from equipment or open flames from blasting, are often absent. For example, in March 2025, a gas explosion, the third in that mining area in 5 years, occurred suddenly in a goaf at the Moranbah North coal mine in Australia, causing the CO concentration to instantaneously exceed 500 ppm. Such incidents, where the ignition source remains unknown, highlight the critical need to identify unconventional, hidden ignition sources within goafs to enhance coal mine safety.

The prevalent consensus suggests that gas explosions are instigated by hot spot ignitions, such as the spontaneous combustion of residual coal or the frictional heating of roof falls [6,7]. However, these explanations often fail to fully account for observations at

---

[*] Corresponding author.
E-mail address: dmwangcumt@outlook.com (D. Wang).

https://doi.org/10.1016/j.ijmst.2025.09.003

accident sites. For instance, there are frequently no precursory indicators of spontaneous coal combustion, such as overruns of temperature and CO, or C_2H_4 before a gas explosion. In addition, the temperatures generated by the impact and friction of hard roof falls typically remain below 300 °C, insufficient to reach the minimum methane ignition temperature of 600 °C [8]. Notably, a correlation exists between gas explosions and coal-rock dynamic phenomena or mine pressure appearance [9]. For instance, a gas explosion occurred at the Daping coal mine in Henan Province in 2004, triggered by a coal and gas outburst. Similarly, a mine quake initiated a gas explosion at the Sunjiawan coal mine in Liaoning Province in 2005. Furthermore, a correlation exists between gas explosion or combustion events and roof collapse during the initial and periodic weighting, as listed in Table 1. These events suggest that the release of thermal and electromagnetic energy from the substantial strain energy associated with roof deformation and fracture may provide an ignition source [10]. Although previous studies have investigated frictional hot spot ignition from fractured rocks, the potential for electrical ignition of methane/air mixtures by rock fracturing has not been adequately explored.

Rock damage and fracture under stress generate a range of electrical signals, including induced charge, electromagnetic radiation, electric potential, and microcurrents [11,12]. These signals are used to characterize the extent of rock mass damage and fracture, aiding in the prediction of earthquakes and coal-rock dynamics disasters [13]. The electrical signals generated by rock damage processes are involved in the generation, accumulation, and release of internal free charges [14]. The intensity of these signals is influenced by factors such as the physical and mechanical properties of rocks, applied stresses, temperature, and moisture content [15,16]. These free charges can migrate through internal rock defects and also escape into the surrounding environment during loading [17]. The interaction of these charged particles with ambient gases results in luminous emission, which is described as an electric spark [18]. Toshihiko et al. [19] found that only the fracturing of quartz-bearing rocks emitted significant visible light when comparing the luminous emissions from the fracture of quartz-bearing quartz sandstone and granite to quartz-free basalt. Similarly, Matelli et al. [20] observed that luminous emissions from areas of collapsed and fragmented rock, which they attributed to free charge movement. Brady et al. [21] determined the spectra of rock luminescence in argon, helium, and water environments, finding that the spectral bands corresponded to the spectral lines of the surrounding ambient gas molecules. This luminous emission is thought to arise from free electrons released from rock fractures bombarding the surrounding gas [22]. The energy of the high-energy electrons emitted was derived from the potent electric field owing to the rock fracturing [23]. Widom et al. [24] showed that mechanical energy was converted into electrical energy through the piezoelectric effect during rock fracture, leading to the acceleration of condensed electrons and subsequent collisions that release energy. Likewise, Takaki and Ikeya [25] attributed luminous emission to the release of compensated bound charges due to strong electric fields at the fracture. Lockner et al. [26] proposed that rock shear friction induces charge separation and the formation of strong electric fields, ultimately triggering discharge luminescence. Freund [11] concluded that natural semiconductor batteries can form during rock loading, with corona discharge ionizing the air to create an ionic current. Enomoto [27,28] discovered that the gas surrounding newly formed cracks carries a negative charge during rock loading, attributed to the emission of unpaired electrons in the presence of a piezoelectric field. Moreover, they suggested a causal relationship between multiple earthquake-triggered fires and the release and combustion of methane from the underground. The static electricity generated by the flow of charged gas during rock fracture may also provide an ignition source during earthquakes [29]. In recent years, Li et al. [30,31] have noted a possible link between gas explosions and roof fracture discharges in goafs. They have conducted a preliminary investigation into the generation of electrical sparks from the fracture of different lithology sandstones in an air atmosphere. However, direct validation of the potential for roof fracturing to ignite methane/air premixed gas remains lacking.

In conclusion, the ignition cause of gas explosions induced by roof collapse in coal mines remains unclear. This study will focus on electric ignition by rock fracturing, as a new perspective differing from the conventional thermal ignition theory. To this end, a rock-fracturing ignition experimental system was constructed by combining a mechanical loading system and a gas explosion chamber. Furthermore, comprehensively employing electrical-optical monitoring techniques, the relationship between the electrical signal response, luminous emissions of sandstone fracturing and the gas explosion under tensile and compressive fractures was analyzed. Ultimately, the study aims to verify the possibility of igniting premixed gases induced by roof sandstone fracturing under stress, and clarify the electric ignition mechanism in a gas explosion. This research is expected to provide new insights and a theoretical foundation for the prevention and control of gas explosions in coal mines.

2. Experimental system and scheme

2.1. Specimen preparation

Sandstone serves as a key roof in coal mines, bearing the weight of overlying pressure. Four sandstones were selected from two coal mines, Xieqiao in Anhui and Xiakatan in Xinjiang, which have experienced gas explosions. The sandstones with different lithologies were classified as sandy mudstone (SM), fine sandstone (FS),

Table 1
Gas explosions or combustion incidents during roof fracture in coal mines in China.

Time	Coal mine	Results	Main roof	Roof fracture
14/02/1999	Qitaihe	A gas explosion during roof caving in a goaf, causing 48 deaths	Gritstone	Periodic weighting
24/10/2003	Baijigou	A gas explosion during the roof caving in a goaf, causing four burns	Gritstone	Periodic weighting
04/06/2011	Rujigou	There was a gas combustion above a hydraulic support	Fine sandstone	Periodic weighting
29/03/2013	Babao	A gas explosion during the roof caving in a goaf, causing 51 deaths	Quartz sandstone	First weighting
08/04/2013	Xiakuotan	A gas explosion during the roof caving in a goaf, causing 10 burns	Quartz sandstone	Periodic weighting
30/10/2015	Xinjie	A gas explosion during the roof caving in a goaf	Quartz sandstone	Periodic weighting
23/03/2016	Anping	A gas explosion during the roof caving in a goaf, causing 20 deaths	Gritstone	Periodic weighting
15/03/2019	Dongshengyangsheng	A gas explosion occurred during the roof caving in an upper corner	Fine sandstone	First weighting
11/03/2024	Xieqiao	A gas explosion during the roof caving in a goaf, causing 9 deaths	Fine sandstone	Periodic weighting

gritstone (GS), and quartz sandstone (QS), respectively. Rock blocks extracted from the working faces were then processed into cylindrical (φ50 mm × 100 mm) and disc-shaped (φ50 mm × 25 mm) specimens, as shown in Fig. 1. The surface roughness of each specimen was polished to below ±0.05 mm to minimize stress concentrations during testing. Ultrasonic wave velocity detection was used to screen out specimens with abnormal internal structures. The selected samples were then dried in a vacuum oven at 80 °C for 24 h to eliminate the influence of external moisture. Eight homogeneous sandstone specimens of each lithology were divided into two groups for subsequent Brazilian splitting (BST) and uniaxial compression testing (UCT). The average densities of the four sandstone types ranged from 1.87 to 2.58 g/cm^3, the average compressive strengths ranged from 35.39 to 171.41 MPa, and the average tensile strengths ranged from 2.51 to 9.57 MPa, as shown in Table 2. X-ray diffraction analysis (Fig. 2) revealed that the sandstones were primarily composed of quartz, albite, microcline, and kaolinite, with quartz content varying from 21.3% to 78.4%. This compositional range is representative of typical sandstones found in coal mines [32].

2.2. Experimental equipment

A dedicated experimental system was established to characterize the ignition ability of methane/air premixed gas by discharge of rock deformation and fracture, as shown in Fig. 3. The core components of the system include a mechanical loading system, an electrical signal acquisition system, an optical signal detection system, a high-speed camera, and an explosion reaction chamber.

The mechanical loading system consists of an MTS-YAW4206 electro-hydraulic servo testing machine and its console. This system has a maximum loading capacity of 2000 kN and a loading accuracy of ±1%. The loading acquisition frequency was set to 0.03 s^{-1}. The system can be adapted for BST and UCT experiments by changing the press fixtures (Fig. 3a).

The electrical signal acquisition system utilizes a Keithley DMM6500 digital multimeter with a measurement range of 100 nV–1000 V and a sampling frequency of 0.03 s^{-1}. The custom PC software was used to record high-precision electrical data from the rock specimens during loading.

The photoelectric detection system is composed of a photomultiplier sensor (PDA10A2) and its associated data acquisition software (DAQSensor). The photomultiplier sensor converts optical signals into voltage outputs (0–5 V) with a maximum sampling rate of 50000 sps/s.

The explosion reaction system comprises an explosion chamber, methane and air supply cylinders, flow meters, a pressure transducer, a gas concentration meter, and a vacuum pump. The explosion chamber measures 100 cm × 45 cm × 45 cm with 1 cm-thick cast steel walls. The front of the chamber is equipped with a 1.5 cm-thick explosion-proof quartz glass to detect luminous emission and gas explosions using a high-speed camera (Phantom VEO-710) and photoelectric detectors. A 150 mm-diameter pressure release port, sealed with a rubber piston, is located at the rear of the chamber. To prevent sparks from rock-to-metal contact, the chamber walls, indenter, and gaskets were coated with insulating glue.

2.3. Experimental procedure

The experiments were conducted under the following laboratory conditions: initial temperature of 25.3 °C, initial pressure of 101325 Pa, and relative humidity of 34%. Electrical signals, luminous emissions, and ignition of rock fractures were investigated in methane/air premixed gas. The experimental procedure is as follows.

(1) Rock specimens were positioned under the indenter and subjected to UCT and BST with a low loading rate of 2 and 0.2 kN/s to avoid dynamic distortion caused by the

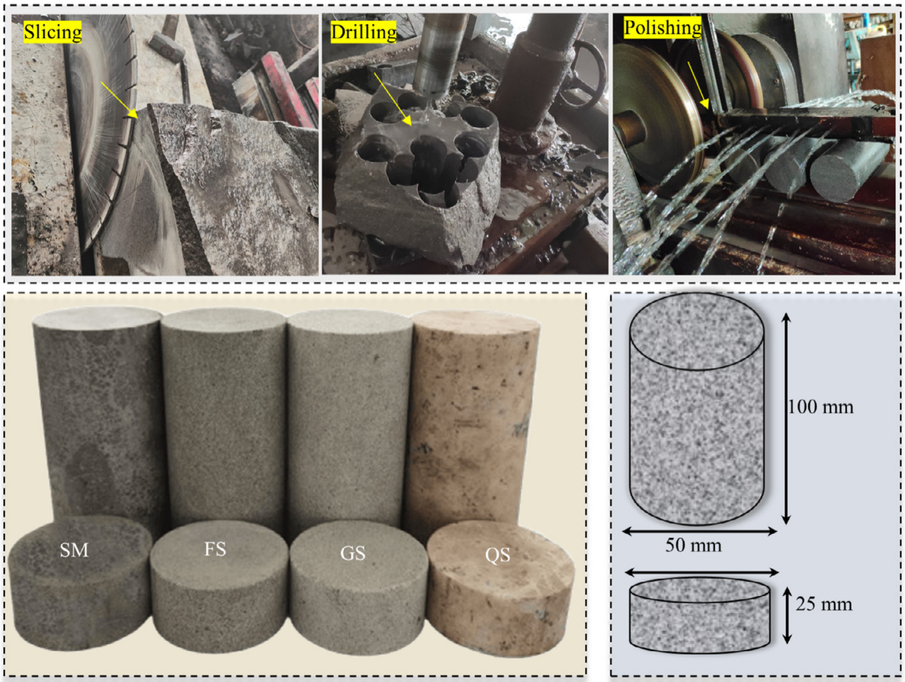

Fig. 1. Preparation process of specimens.

Table 2
Physical and mechanical parameters of sandstones.

Lithology	Nomenclature	Coal mine	Average density (g/cm^3)	Average compressive strength (MPa)	Average tensile strength (MPa)	Size φ mm × mm
Sandy mudstone	SM	Xieqiao	1.87	35.39	2.51	50×100 50×25
Fine sandstone	FS	Xieqiao	2.43	126.54	5.28	50×100 50×25
Gritstone	GS	Xiakuotan	2.37	56.57	3.14	50×100 50×25
Quartz sandstone	QS	Xiakuotan	2.58	171.41	9.47	50×100 50×25

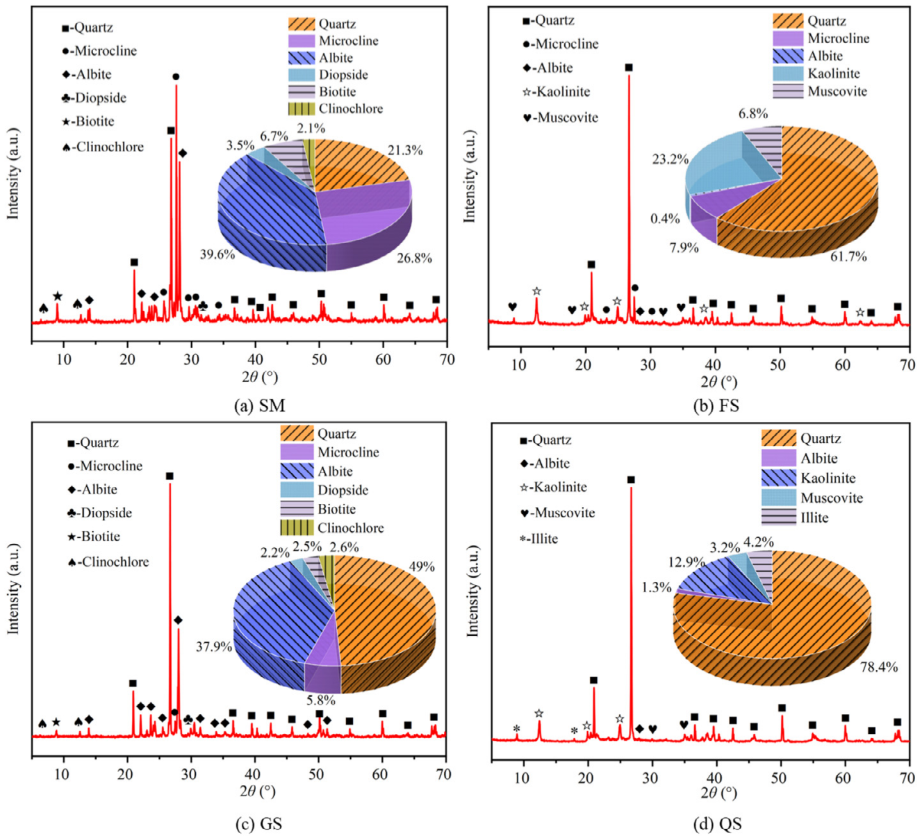

Fig. 2. Mineral composition and content of sandstones.

inertia effect, respectively, as illustrated in Fig. 4. An insulating paper with a surface resistance of 2.4 MΩ was placed between the rock specimen and the indenter to mitigate external electromagnetic interference. Two sets of monitoring points were arranged separately to evaluate the charge generation and discharge capacity of the rock specimens, as shown in Fig. 4. The first set of measurement point (A1) was placed at both ends of the specimen, with sensors in direct contact with the specimen surface to measure surface voltage generated by internal charge accumulation and transport. The second set of measurement points (A2) used a copper sheet suspended 1 mm from the specimen surface to capture charge transfer to the ambient gas during rock fracture. The conductive copper plate (30 mm × 30 mm) was mounted on an insulating bracket. Therefore, the surface voltage reflects the ability to generate and accumulate charges of rocks, while the external voltage is employed to characterize the discharge intensity.

(2) The chamber was evacuated to −0.06 MPa before admitting methane/air mixtures. Gas flows were regulated to achieve a methane concentration of 9.5% (±0.1%) in the mixture. Methane exhibits its lowest minimum ignition energy and highest explosive intensity at its stoichiometric concentration (approximately 9.5%) [33]. This specific condition represents the most hazardous scenario for coal mine gas explosions. The valves were then closed, and the mixture was allowed to stabilize at atmospheric pressure for 10 min to ensure homogeneity.
(3) The high-speed camera and photodetector were placed at the front of the window to capture the light emission and ignition process when the rock was subjected to external loads in the dark. The resolution of the camera was set at 1280×800, and the frame rate was set at 2000 fps. The sampling frequency of the photoelectric probe was set at 10000 sps/s
(4) BST and UCT experiments were performed at prescribed loading rates while all monitoring systems were active. If rock fracturing initiated a gas explosion, the resulting shock-

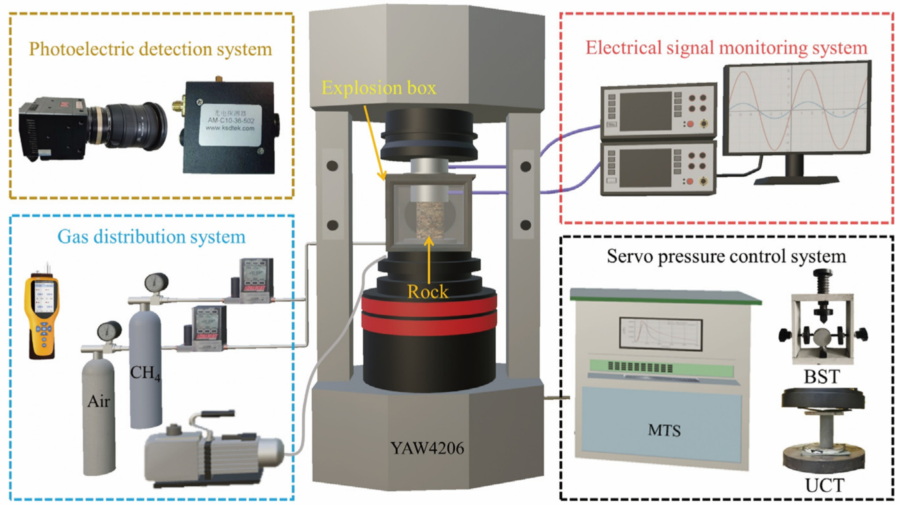

(a) Schematic diagram

(b) Physical drawing

Fig. 3. Discharge ignition system by rock fracturing under loading.

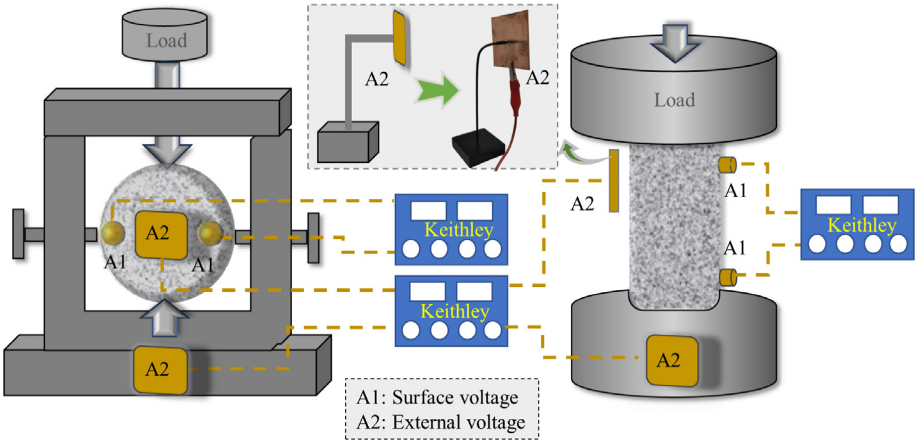

Fig. 4. Monitoring point layout of electrical signals under BST and UCT experiments.

wave would fracture the piston for active venting. Otherwise, the relief port was manually opened to purge the chamber gases before repeating the test.

3. Results

3.1. Electrical signal response to sandstones during deformation and fracture

Electric signals are detected in the rock surface and the surrounding gas environment during rock deformation and fracture [34]. Surface and external voltage reflect the ability to charge generation and release of rocks, respectively. Fig. 5 shows the surface and external voltage changes over time during the tensile fracture of various lithological samples. The voltage responded significantly to the applied loading, particularly the surface voltage. The change of surface and external voltage was mainly divided into two stages: a slow increase (Stage I) followed by a sudden rise (Stage II), both of which were related to the damage of the rock. Specifically, uniaxial stress induced dipole realignment in polar quartz crystals, generating piezoelectric polarization during elastic and plastic deformation phases [35]. As quartz crystals were damaged, the bound charges were converted into free charges, which were then transferred to the rock surface. The quartz contents of SM, GS, FS, and QS were 21.3%, 49.0%, 61.7% and 78.4%, respectively. At Stage I, the surface voltage of the four sandstones was 0.0001–0.0137, 0.0001–0.0145, 0.0002–0.0217, and 0.0002–0.0819 V, respectively. This change was positively correlated with the quartz content. In addition, the uneven spread of primary pores and microfractures in rocks led to a continuous increase in the number of defect structures. Significant deformation induced crack propagation, breaking numerous atomic and molecular chemical bonds [36]. This process generates dangling bonds that produce new static or free charges. The deformation and damage of the microstructure thus contribute to a gradual increase in the surface and external voltage of the rock. Yet, the voltage changes in Stage I were not linear but fluctuating, possibly owing to the undirected flow of internal free charges. Charge accumulation and release occurred concurrently, hindering the maintenance of high free charge density in a localized crack region. During complete rock failure, marked by a rapid load drop, transient surges emerge in both surface and external potentials, exhibiting significant voltage peaks. These surges reflect massive charge liberation during tensile fracture, followed by its transport to rock surfaces and subsequent discharge into the surrounding gas. During Stage II, the sandstone underwent a main fracture, causing a spike in surface and external voltages, followed by a sharp decline. The intergranular and transgranular fracture of quartz crystals released a substantial amount of bound charge. Free charges previously concentrated at crack tips were instantaneously released. Besides, the propagation rate of microcracks between mineral grains and their cementing materials accelerates, leading to the formation of macroscopic fractures. Free charges generated by crack propagation were thereby transferred from the crack surfaces or tips to the specimen surface and the external gas. The peak surface voltages of the SM, FS, GS, and QS specimens were 0.075, 0.175, 0.104, and 0.874 V, respectively. Additionally, the peak external voltages of four sandstones were 0.024, 0.043, 0.031, and 0.144 V. The charge generation and release capacity of the FS and QS specimens exceeded that of the SM and GS specimens.

The surface and external voltage of sandstones exhibited similar phase changes under uniaxial compression, as depicted in Fig. 6. The change trend of surface voltage during the uniaxial compression was more significant than that of tensile fracture. Notably, a clear rising trend was observed in the surface voltages of QS-1 and FS-2 specimens during the plastic deformation stage. During Stage I, the surface voltages of the SM, GS, FS, and QS specimens ranged from 0.0001 to 0.02126, 0.0001–0.0243, 0.0002–0.0956,

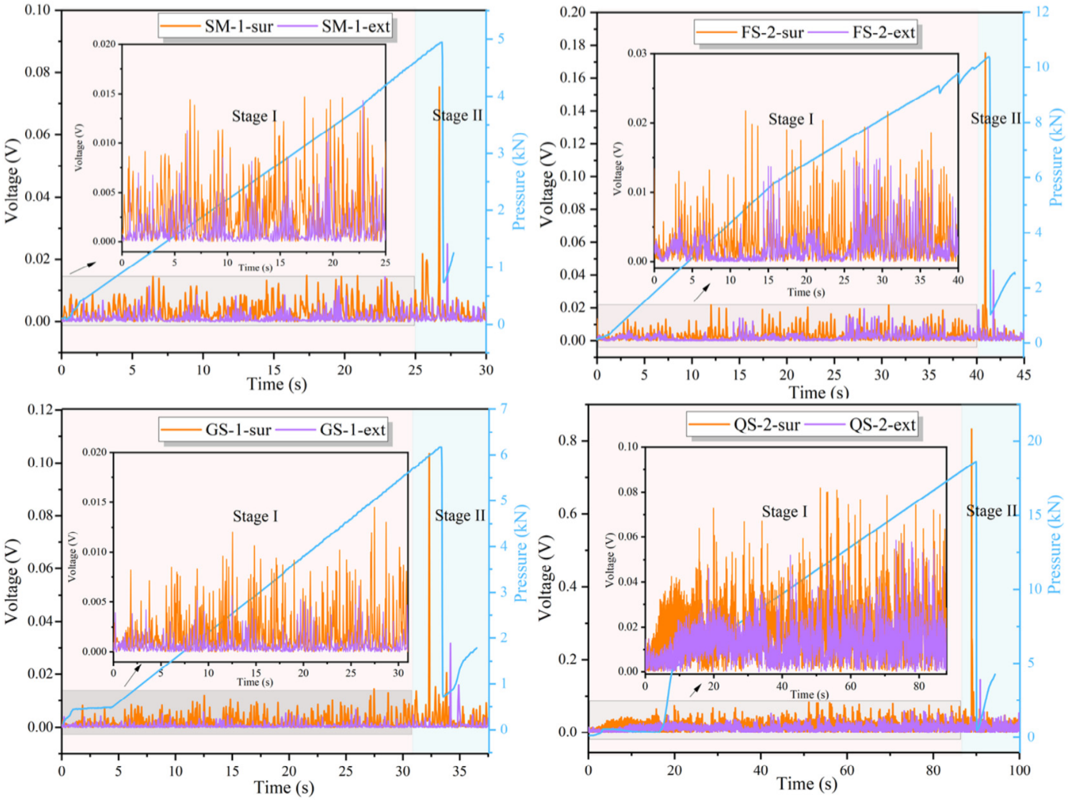

Fig. 5. Surface and external voltage of sandstones under the BST experiment.

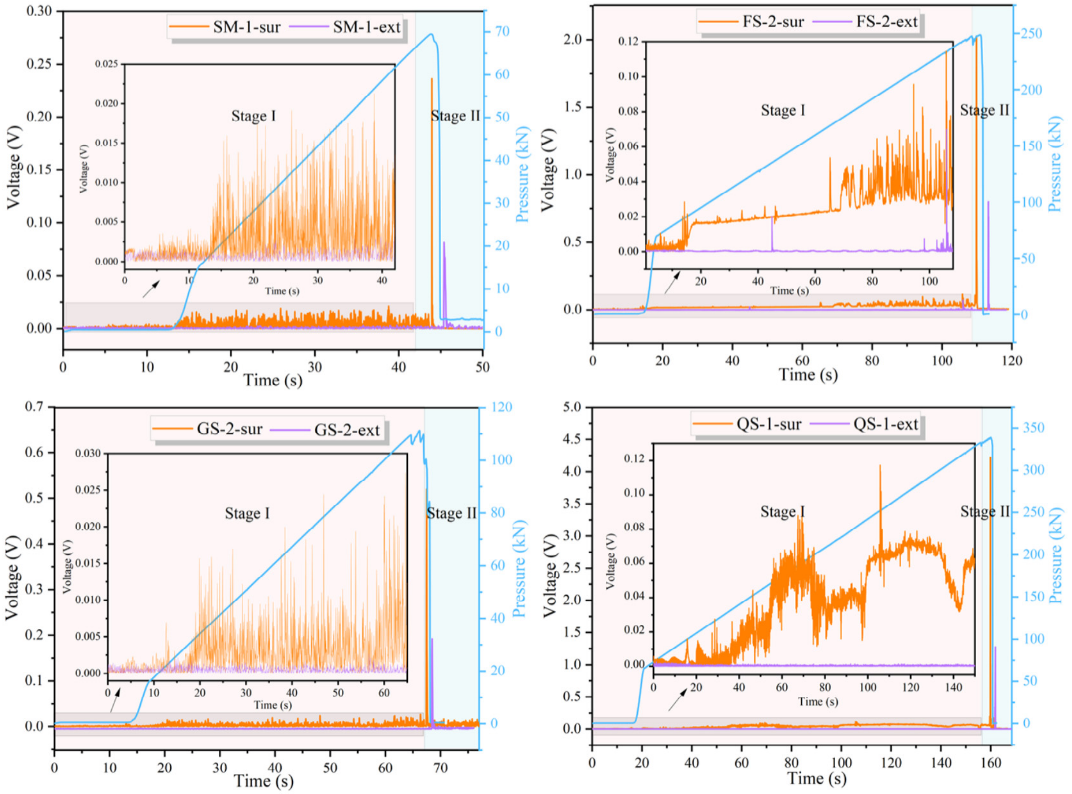

Fig. 6. Surface and external voltage of sandstones under the UCT experiment.

and 0.0003–0.1174 V, respectively. The surface voltages of FS and QS samples were 4–5 times higher than those of SM and GS samples. At Stage II, the peak surface voltages of the SM, GS, FS, and QS specimens were 0.236, 0.52, 2.028, and 4.223 V, respectively. This trend is similar to that of the disc sandstones. Moreover, the external voltages of the four sandstones were 0.081, 0.224, 0.8, and 1.275 V. The larger the peak surface voltage of the rock samples, the larger the peak external voltage. Fig. 7 shows a strong correlation between the surface voltage and external voltage with a correlation coefficient of 0.9664. This demonstrates that bound charges accumulated on rock surfaces overcome the surface potential barrier under electric fields and escape to the surrounding gas environment, thus establishing an external potential difference. Furthermore, this indicates a significant portion of free charge remains trapped on the rock surface, requiring a higher energy for escape into the surrounding gaseous environment.

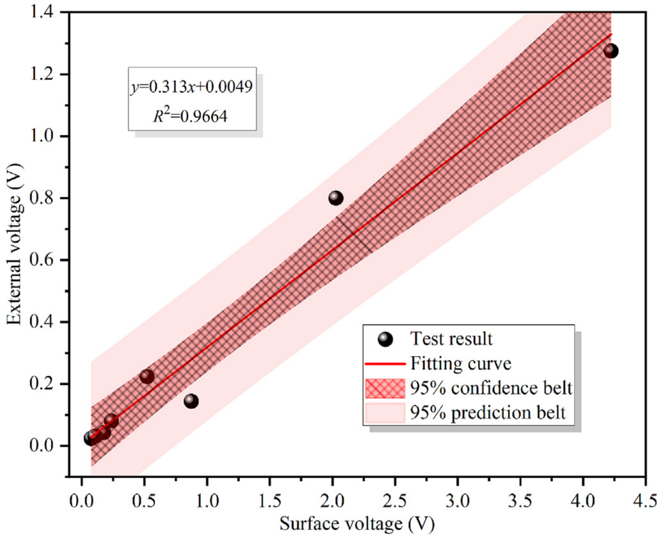

Fig. 7. Connection between surface voltage and external voltage of sandstones.

The surface voltages of sandstone under uniaxial compression were significantly higher than those during tensile fracture at Stages I and II. Specifically, peak surface voltages in cylindrical specimens were 4–12 times higher than in disk specimens. Given that the tensile strength of sandstones was significantly lower than their compressive strength (Table 1), the plastic deformation and fracture are more intense under the UCT compared to the BST. Longer loading periods in sandstone promote the nucleation and propagation of dislocations and cleavages between mineral particles, which in turn enhance free charge generation and accumulation. Notably, external electrons were detected earlier in disk samples at Stage I, and their external voltage signal exhibited greater amplitude than in cylinder samples. This is attributed to the copper sheet effectively capturing the escaped electrons from the crack, facilitated by the single propagation path in the disk samples. Conversely, the crack distribution in compressed cylindrical specimens is more complex during plastic deformation, potentially resulting in a lack of crack development in the area where the copper sheet is positioned. However, the amount of free charge released during compressive fracture substantially exceeds that released during tensile fracture. As a result, the cylinder specimen exhibited 3–9 times higher peak external voltage than the disk specimen during Stage II. This difference arises from the formation of multiple cracks during failure, as further analyzed in Section 4.1.

3.2. Luminous emission and ignition properties of sandstone fractures

The interaction between free electrons released by rock fracture and ambient gas molecules triggers the luminous emission [37].

Luminescence by rock fracture is a transient event with a slight luminous intensity. Hence, luminescence is most readily observed in dark conditions. An opaque black curtain was utilized to wrap the entire explosion chamber to eliminate external light interference. Additionally, pre-experiments revealed that the collision of fractured rock with the metal box could generate splattered iron oxide fragments. To mitigate this potential interference, insulating glue was applied to the box walls.

Distinct variations in luminous emission were observed among different sandstone lithologies during tensile failure. Luminous emission coincided with the coalescence of tensile cracks in disc specimens, leading to complete failure. However, neither high-speed camera nor photodetection captured visible light during the tensile failure of SM and GS disks. This absence may be attributed to their low tensile strength, where rapid fracture kinetics preclude sufficient charge accumulation and release. The probability of luminescence for the FS and QS discs was 50% and 75%, respectively, owing to the inhomogeneity of the specimens. Fig. 8 exhibits representative luminous emission for FS and QS disks. It can be seen that the light was emitted along the cracks along the center of the disk. This observation indicates a correlation between luminous emission and crack initiation and propagation. In addition, the peak luminous emission intensity, converted to electrical signals, ranged from 0.247 to 0.726 V, with a duration of approximately 0.5 ms. The more pronounced luminous emission observed in quartz sandstone may be attributed to an enhanced piezoelectric effect.

Fig. 9 exhibits typical luminous emissions of the SM, GS, FS, and QS cylindrical specimens in UCT experiments, and the frequency of their luminous emissions is 25%, 25%, 75%, and 100% in the four repeated experiments. Similar to the disk specimens, spark propagation in the cylindrical specimens extended from internal defect surfaces to the rock surface. This observation reinforces the conclusion that luminous emission originates from the rock fracture surface, distinct from the metal indenter and chamber. Furthermore, the location and color of the sparks differed significantly from those of iron oxide fragments, which exhibit a bright yellow color owing to high-temperature oxidation of iron. In contrast, the sparks from rock fracture displayed yellow and orange hues, related to the surrounding gaseous media [38]. Weak luminous emissions were observed in the plastic deformation in the UCT experiments when microcrack coalescence into localized fracture surfaces, especially in SM specimens. Nevertheless, the obvious luminous emission mainly occurred in the complete failure of sandstones. The peak luminous intensity of the SM, FS, GS, and QS samples was 0.47, 1.154, 0.754, and 2.256 V, respectively, with corresponding durations of 2.5, 10, 1.5, and 7.5 ms. The intensity and duration of the luminescence of the FS and QS specimens were significantly higher than that of the SM and GS specimens. Additionally, luminous emission from the sandstones by compression fracture was stronger than that from the tensile fracture specimens, as shown in Figs. 8 and 9. This tendency is consistent with the fluctuation of electrical signals observed in sandstones in Figs. 5 and 6. This increased luminous emission intensity during compres-

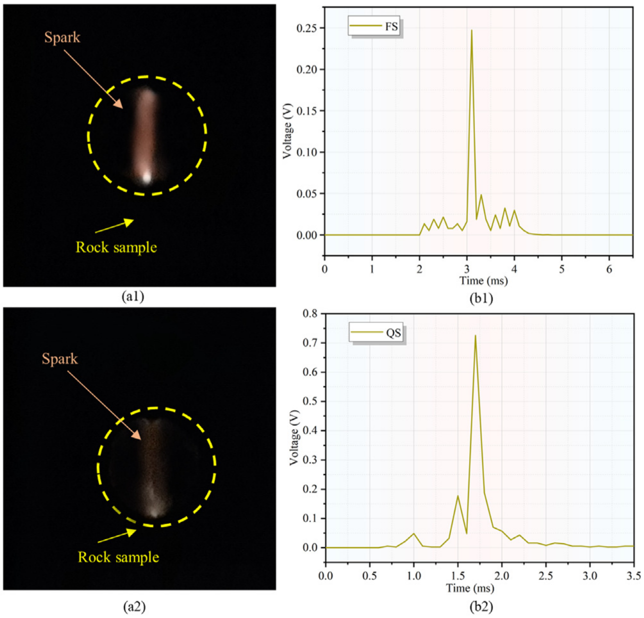

(a) Luminous morphology (b) Luminous intensity

Fig. 8. Luminous emission from rocks at tensile fracture.

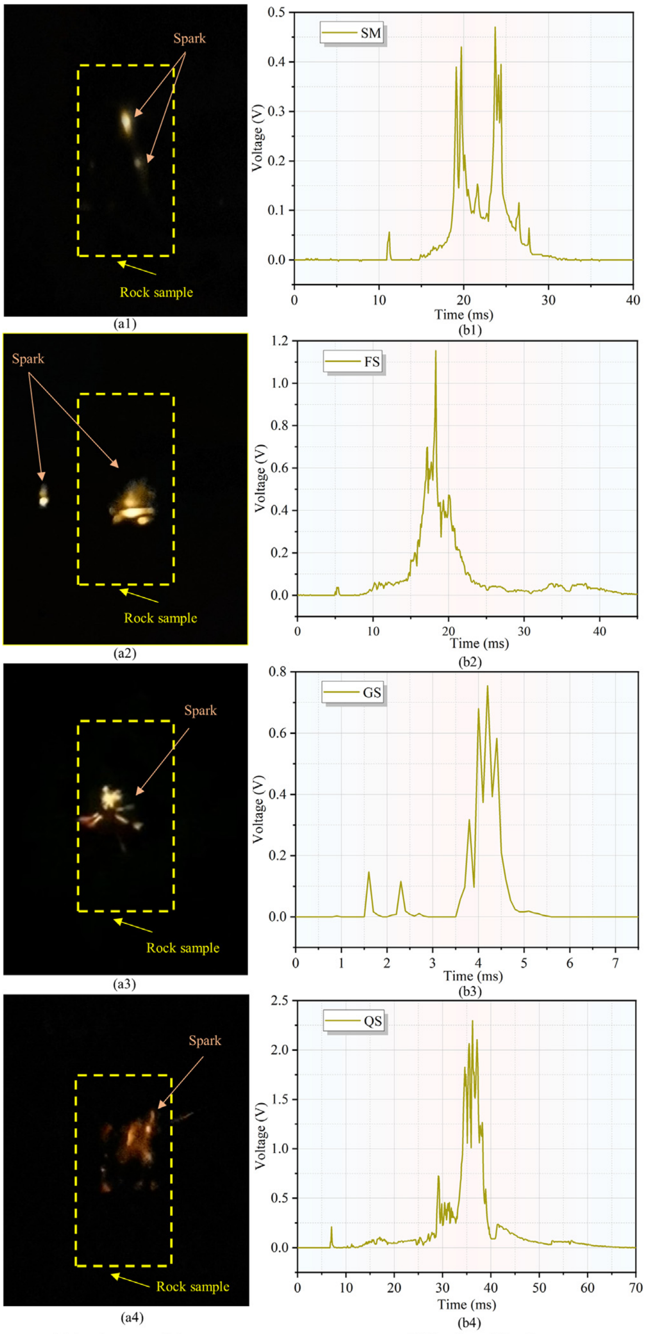

(a) Luminous morphology (b) Luminous intensity

Fig. 9. Luminous emission from rocks at compression fracture.

sion fracture is likely owing to the enhanced charge release within rocks. Fig. 10 illustrates the linear relationship between the luminous emission intensity and the peak surface and external voltage, with a relative coefficient of 0.9695 and 0.9429, respectively. This finding further confirms that free electron motion is the source of the luminous emission.

Variations in discharge and luminescence intensity are influenced by the physical and mechanical properties of the rocks. While compressively fractured FS and QS specimens triggered gas explosions, tensile fractured specimens failed to ignite the methane/air premixed gas. However, gas explosion flames generated light signals exceeding photodetector ranges, precluding quantitative comparison.

Figs. 11 and 12 depict the temporal development of a gas explosion caused by FS and QS specimens during the compression fracture, respectively. The initial flame core of the gas explosion originated at the rock crack surface or tip, as shown in Figs. 11b and 12b, spatially coinciding with the observed luminous emission. This finding confirms that the ignition source was neither iron oxide fragments nor high-temperature rock particles, but rather discharge sparks at the gas-rock interface [39]. Following ignition, the flame, centered on the sandstone specimen, propagated outward in a near-spherical pattern within 50 ms. The flame color transitioned from an initial blue-purple to orange-yellow, accompanied by an acceleration in propagation speed. This evolution signifies the generation of abundant reactive radicals, an accelerated chain reaction rate, and a transition from laminar to turbulent combustion. Subsequently, the flame front became distorted and curled, particularly upon encountering the rough box wall. The gas explosion intensity peaked at 200 ms, as evidenced in Figs. 11f and 12f. Ultimately, the explosion shock wave expelled the rubber piston to depressurize the chamber, leading to flame extinction upon fuel depletion. In addition, quartz sandstone exhibited a slightly higher initial ignitability than fine sandstone. This conclusion is supported by the easier formation of the critical orange flame kernel observed in Fig. 12b.

4. Discussion

4.1. Ignition mechanism of methane/air premixed gas by discharge and ionization during sandstone fracturing

Rock deformation and fracture under stress may sequentially induce the generation and release of free charges, leading to luminescence and gas explosion as evidenced in Sections 3.1 and 3.2. Consequently, gas explosions triggered by a rock compression fracture are closely related to the motion of these free electrons.

The microstructural deformation, damage, and fracture occur within the rock under loading. Free charges are generated and accumulate due to piezoelectric effects, crack propagation, and friction of sandstones. This explains the gradual increase in surface voltage observed in Figs. 4 and 5 during the plastic deformation stage. When the applied stress exceeds the yield strength, the sandstone undergoes compressive or tensile fracture. This fracture releases high-density free electrons previously trapped within lattice defects, causing abrupt increases in external voltage. Nevertheless, the external voltage ascent lags behind the surface voltage increase, and its peak is consistently lower. This suggests that free charges concentrated at fracture tips require sufficient energy to overcome the surface potential barrier and escape the rock, resulting in discharge. High-energy electrons escaping the rock surface then ionize the surrounding gas molecules, generating luminescence. However, a sustained ionization of a methane and oxygen mixture is necessary to initiate a gas explosion.

Sandstones exhibit variable capacities for generation, accumulation, and discharge of free charges owing to differences in mineral composition and microstructure. Taking compressed fracture specimens as an example, the average, cumulative, and peak surface voltages are positively correlated with quartz content, as demonstrated in Fig. 13. A similar quartz-dependent relationship was observed for external voltage. Hence, the piezoelectric effect of quartz critically governs charge generation and discharge phases within the sandstones. Before macroscopic fracture of the sandstone, localized fracture of quartz crystals releases free charges to the rock surface and surrounding gas, inducing electrical signal fluctuations. Moreover, compression induces polarization of bound charges within the quartz crystal lattice, generating an internal piezoelectric field. This field facilitates the accumulation of abundant free charges, resulting in a high-intensity voltage that enables the escape of high-energy electrons.

The nascent fracture surface of sandstones constitutes a critical region for charge accumulation. As evidenced in Fig. 14, cylindrical specimens fractured under compression exhibit a greater number and width of shear and tensile fractures compared to disk specimens in the BST. These propagating cracks interconnect, forming a complex network that facilitates the accumulation and release of free charges. This enhanced fracture complexity is a primary factor explaining the substantially higher electrical signals observed in compression-fractured specimens relative to tensile-fractured specimens. The pore and microfracture distributions on fracture

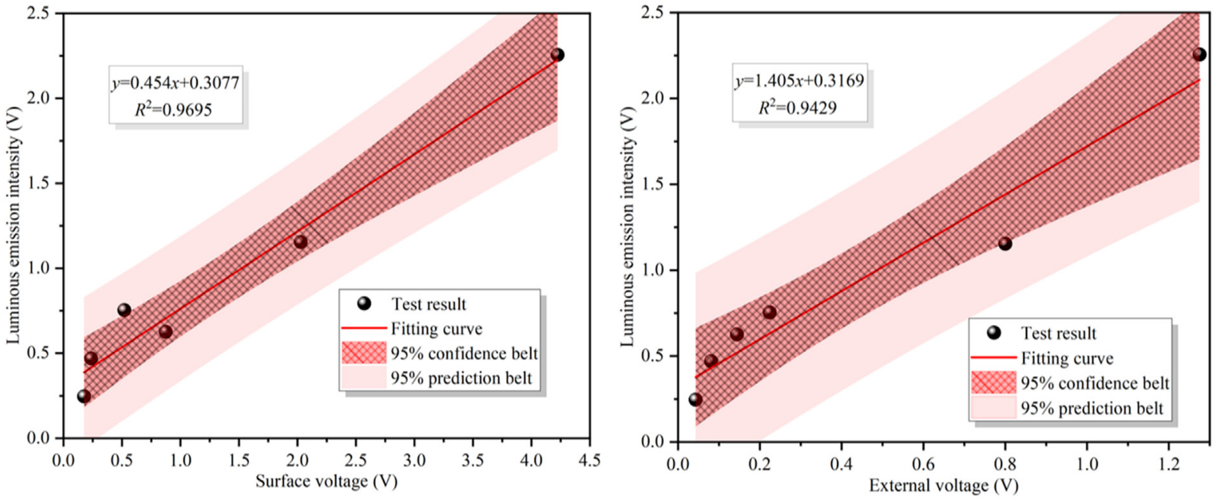

Fig. 10. Connection between luminous emission intensity and the surface and external voltage of rock fracture.

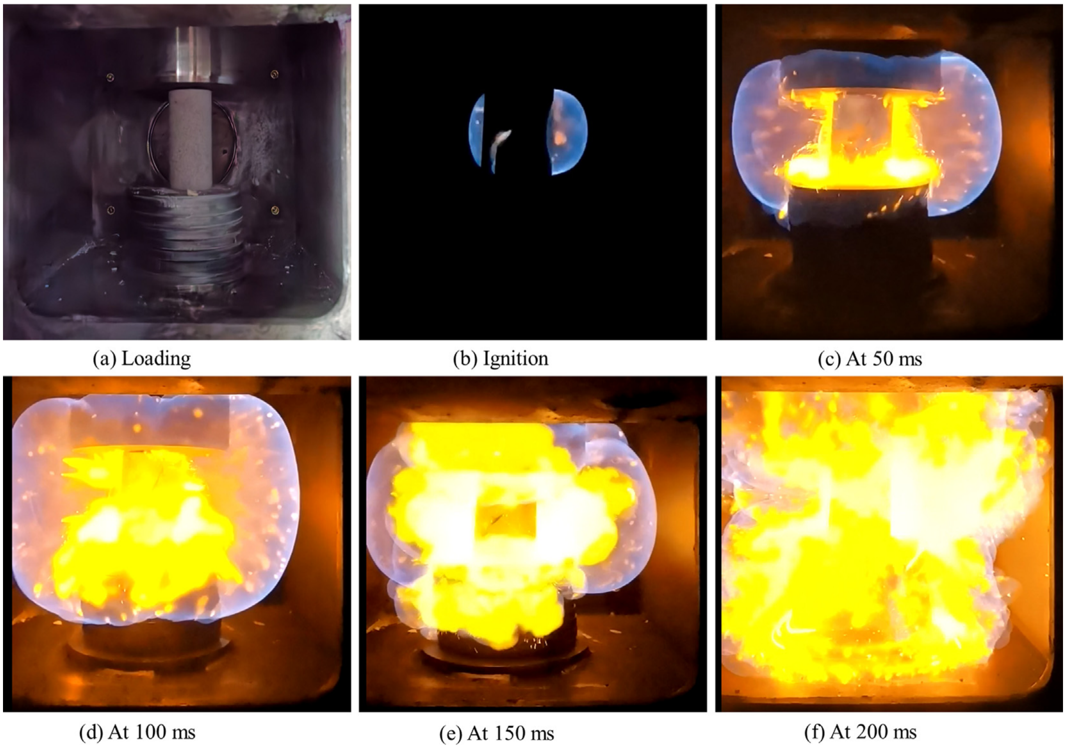
(a) Loading (b) Ignition (c) At 50 ms (d) At 100 ms (e) At 150 ms (f) At 200 ms

Fig. 11. Gas explosion resulted from fine sandstones during the compression fracture.

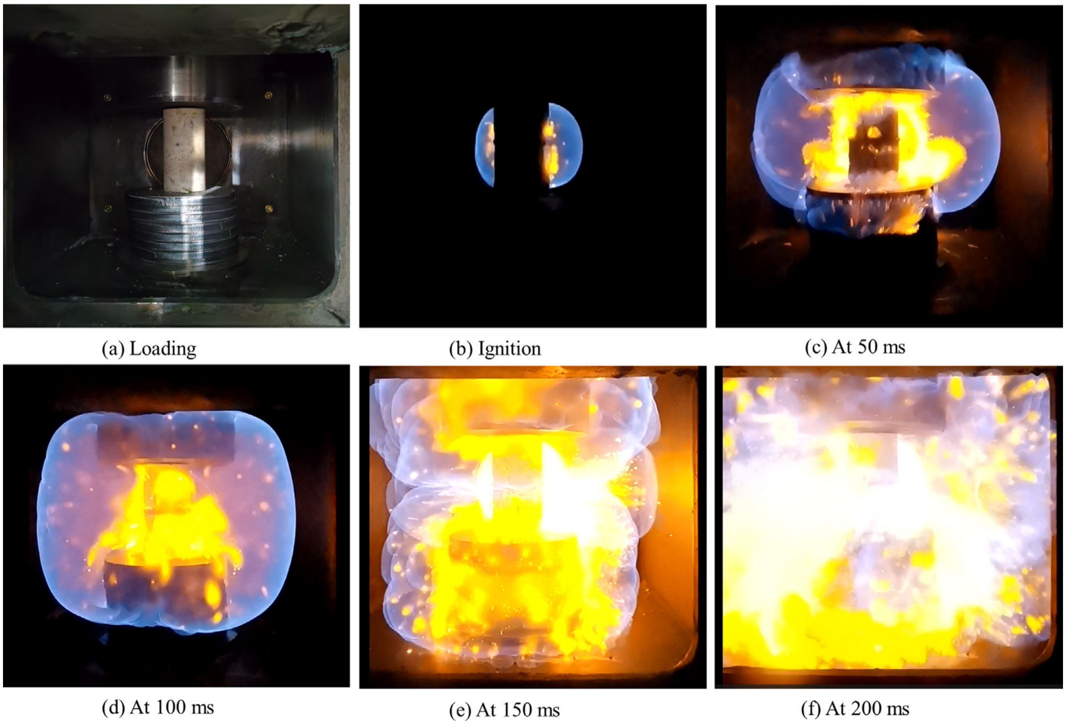
(a) Loading (b) Ignition (c) At 50 ms (d) At 100 ms (e) At 150 ms (f) At 200 ms

Fig. 12. Gas explosion resulted from quartz sandstones during the compression fracture.

surfaces of compression-fractured sandstones before and after being loaded were compared, as shown in Fig. 15. In addition, the contour roughness of fracture surfaces of cylindrical specimens reflects their capacity for triboelectric charging at microscopic defect dislocations, as shown in Fig. 16. The densely distributed primary fractures of sandy mudstone accumulate significant free charges. The dislocation and friction within these pre-existing fractures drive charge movement, partially explaining surface voltage increase during initial uniaxial compression. The interconnection of fractures following fracturing can facilitate charge aggregation and release along fracture surfaces. Conversely, gritstone exhibits tightly interlocked mineral grains with limited microstructural

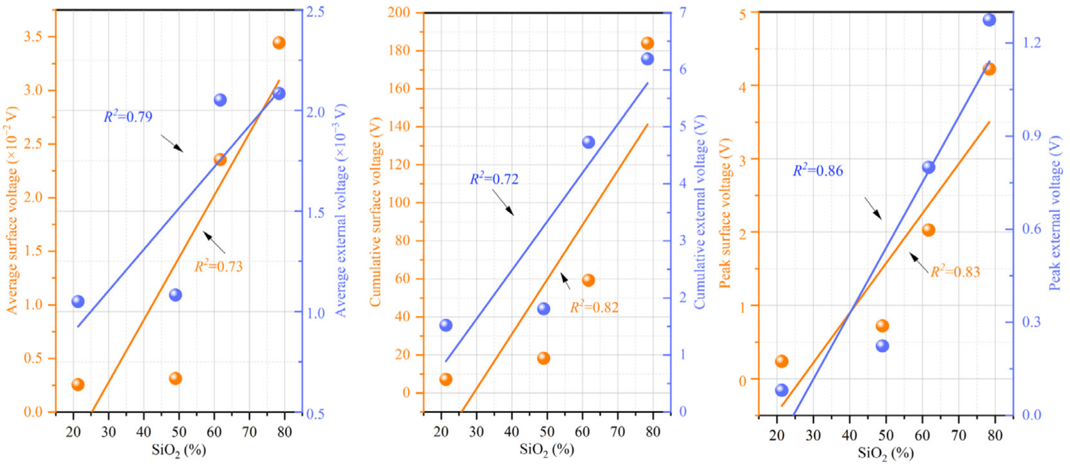

Fig. 13. Connection between surfaces, external voltages and quartz content of sandstones.

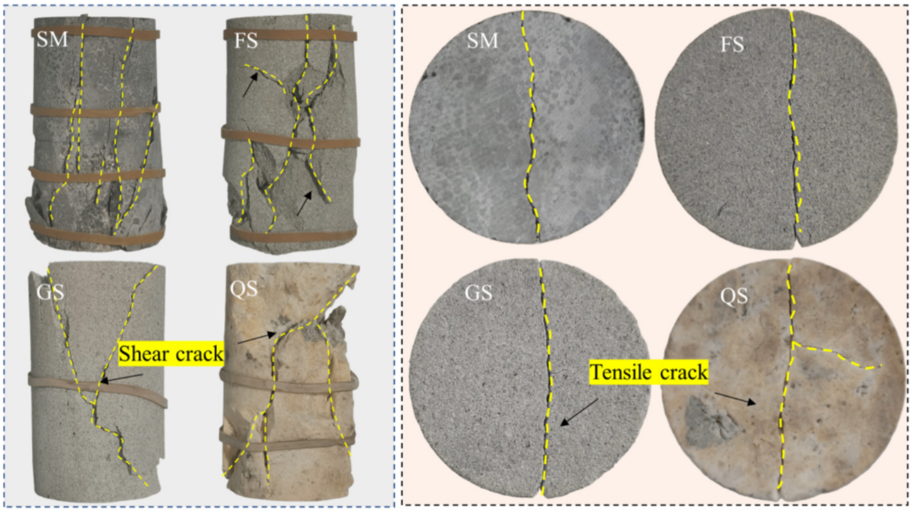

(a) UCT tests (b) BST tests

Fig. 14. Macro-fracture distribution of fractured sandstones.

defects. Surface asperities drive intergranular friction and extrusion, generating electrical signals during the deformation and fracture (Fig. 16c). Fig. 15b and d show that fine and quartz sandstone exhibit homogeneous textures with relatively smooth surfaces, widespread quartz grain distribution, and discrete primary pores. New fractures and pores proliferate while primary pores become interconnected, which enhances free charge generation and accumulation.

Fig. 17a shows a superposed electric field resulting from the piezoelectric effect of fractured quartz crystals, fracture tip effects, and frictional charging at defect dislocations. The strong electric field formed at the crack tip propels high-density free charges from the rock surface into the gas environment (Fig. 17b). These accelerated electrons collide with surrounding gas molecules, leading to luminous emission via high-energy electron bombardment and the excitation and ionization of gas molecules. Specifically, sufficiently energetic escaping electrons collide with gas molecules, forming positive ions and secondary electrons. These liberated electrons subsequently collide with additional gas molecules, inducing further ionization. This chain reaction produces exponential growth in free electron density—the electron avalanche effect (Fig. 17c). Given that the ionization energies of atmospheric constituents are 15.6 eV for nitrogen and 12.2 eV for oxygen, while all four C—H bonds in CH_4 exhibit ionization energies below 4.6 eV [21]. Thus, the high-energy electrons from rock fracturing can readily ionize ambient methane and oxygen molecules. While luminous emission signifies localized gas ionization, sustained ionization of methane and oxygen is a prerequisite for gas explosion initiation. This process generates abundant free radicals that propagate branching chain reactions. Concurrently, localized exothermic reactions preheat the surrounding premixed gas. Rapid thermal expansion of heated gaseous mixtures accelerates ionization through energy transfer. Compressing fractured sandstone can induce light emission. However, the ionization of nitrogen molecules and fracture produce rock dust, which lowers the likelihood of free radical collisions and ultimately results in free radical annihilation and chain termination. The above experiments have revealed that fractures in quartz-rich sandstones (>61%) generate strong electric fields along crack interfaces, enabling sustained excitation of high-energy electrons. These electrons ionize air within fracture gaps, releasing heat. Continued ionization expands the reaction zone to form a critical flame kernel. Radical chain reactions then initiate self-accelerating branched chain reactions, culminating in a gas explosion, as shown in Fig. 17d. Overall,

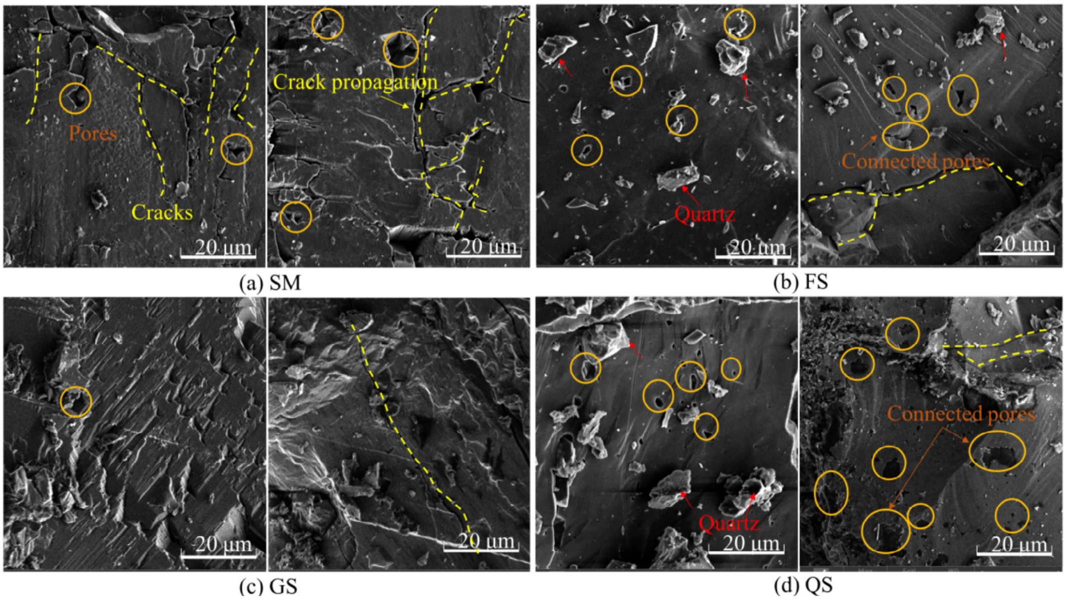

(a) SM (b) FS (c) GS (d) QS

Fig. 15. Microcracks and pores in sandstones before and after loading.

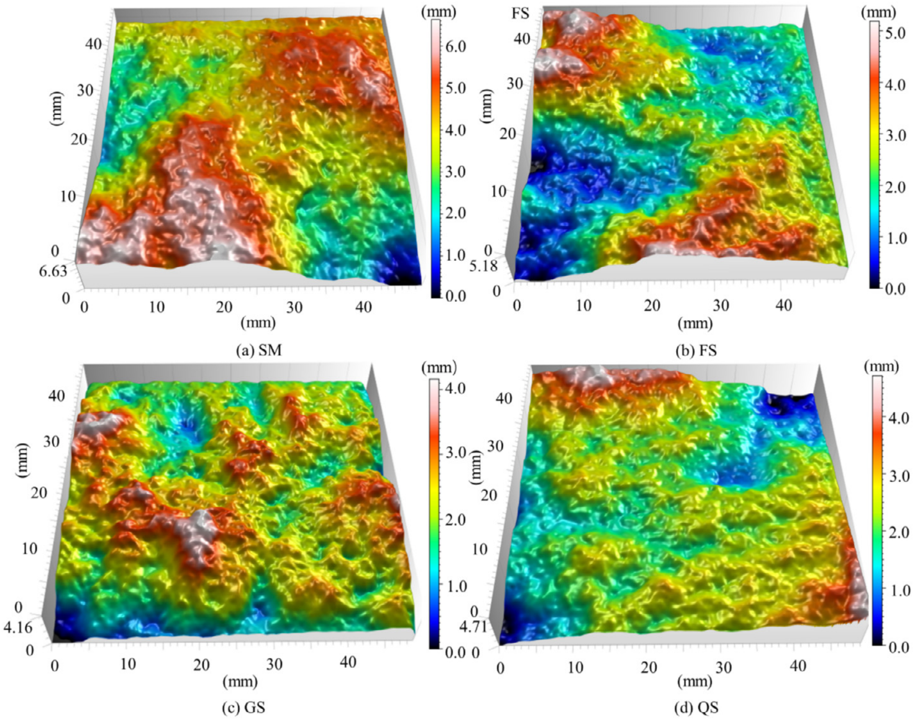

(a) SM (b) FS (c) GS (d) QS

Fig. 16. Three-dimensional morphology of sandstone fracture surfaces.

electrical ignition of rock fracture follows a charge generation-discharge-ionization causative chain. However, other luminescent specimens failed to form a sustained ionization, resulting in the degeneration of flame kernels owing to insufficient discharge energy and duration [40].

4.2. Ignition analysis of a gas explosion in Xieqiao coal mine

On March 8, 2024, a small-scale gas explosion occurred in the upper corner of the 2131(3) working face at the Xieqiao coal mine. Subsequently, a major gas explosion erupted while building the stopping walls in the intake and return airway. This accident resulted in 9 fatalities, destroying stopping walls, mine cars, and gas extraction pipelines within the roadways, as shown in Fig. 18.

4.2.1. Overview of the gas explosion

The Xieqiao coal mine presented several inherent risks, including coal and gas outbursts, spontaneous combustion of mined coal seams, and coal dust explosions. The 2131(3) working face was located in the third stage of the second level mining area. The adjacent 2111(3) and 2121(3) coal faces have been mined out. A coal pillar with 5 m thickness between the 2131(3) and 2121(3) working faces was retained. There was a strike length of 3008 m and an inclined length of 242 m in 2131(3) working faces. The average

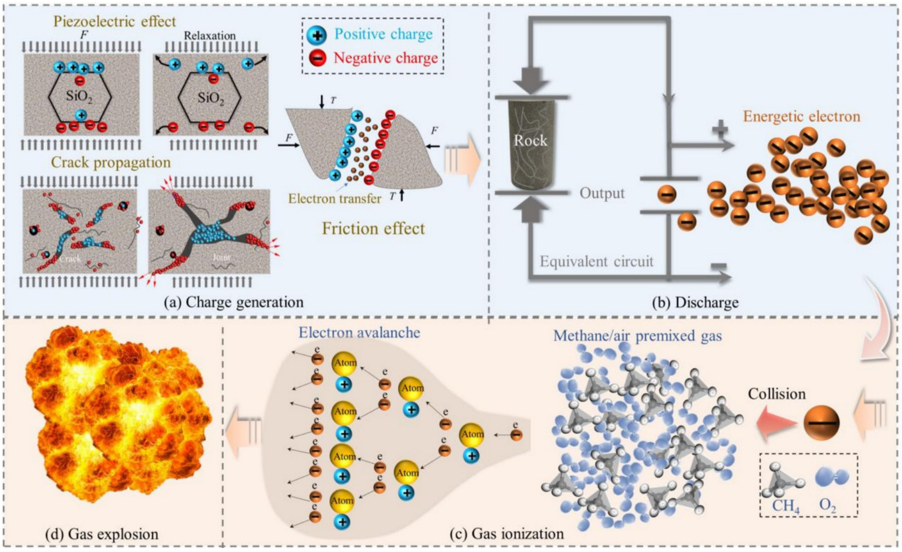

Fig. 17. Ignition mechanisms of methane/air premixed gas by rock fracture discharges.

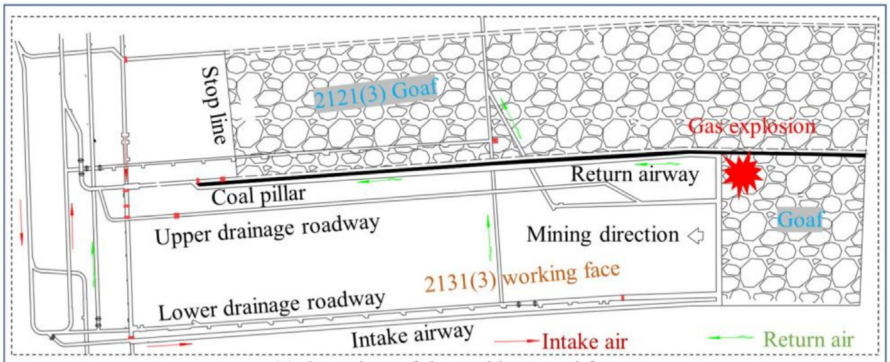

(a) Overview of the accident workface

(b) Destroyed structures and equipment

Fig. 18. Gas explosions in Xieqiao coal mine.

mining height was 6.5 m, and the average inclination angle of the coal seam was 13°.

The 2131(3) working face was formally mined on February 1, 2024, achieving advance rates of approximately 4.0–4.8 m/d. A fault with a 2.2 m drop was encountered in the working face on March 6. On March 8, the initial gas explosion occurred in the upper corner in a goaf, as shown in Fig. 19. The explosion destroyed the filling wall from its interior face outward. Notably, no smoke, open flames, or abnormal phenomena were observed in either the upper corner or return airway before the incident. On March 9, a flame was observed near #60 hydraulic support as a coal cutter cut through the sandy mudstone within the fault. On March 10, a distinct tar odor and visible smoke were detected near #70–94 hydraulic supports. A severe gas explosion occurred when constructing stopping walls in the return and intake roadways on March 11.

4.2.2. Ignition source analysis

Fig. 20 shows that methane concentrations in the goaf persistently range between 8%–15%. The methane originated primarily from faults and adjacent goafs. Oxygen levels maintained above 12% owing to air leakage in the goaf, resulting in a methane-air mixture consistently within the explosive range.

The initial gas explosion on March 8 originated in the upper corner of the goaf, but the ignition source remained unidentified. The remaining ignition source subsequently triggered a catastrophic explosion during sealing operations. Therefore, identifying the initial ignition source is of paramount importance for future preven-

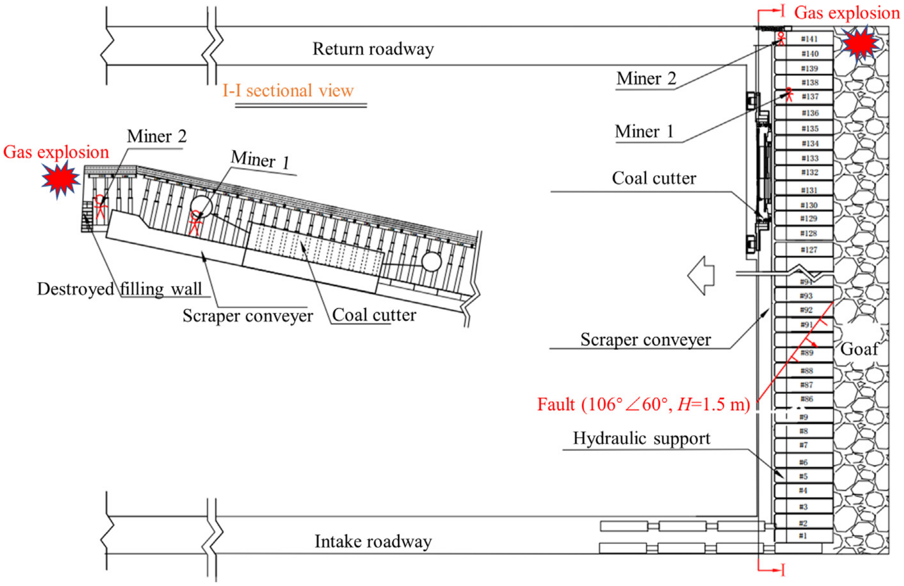

Fig. 19. Field situation in first gas explosion in the goaf in Xieqiao coal mine.

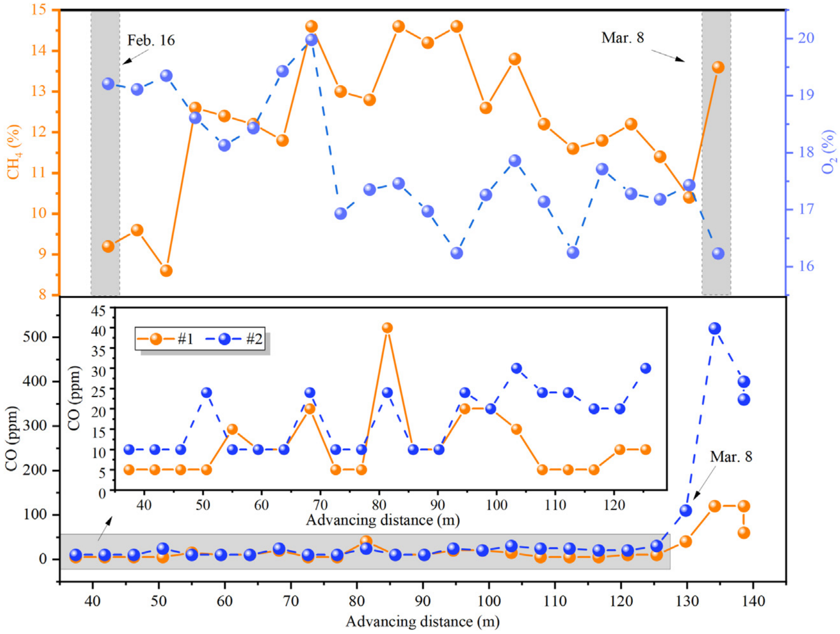

Fig. 20. Change in gas concentration in the goaf.

tion efforts. There was no filling of polymer material, no blasting operations and no chipping of anchors or anchor rods in the goaf. Therefore, potential ignition sources include spontaneous coal combustion, friction sparks between the coal cutter and rock, and electrical ignition resulting from roof rock fracture.

(1) Coal spontaneous combustion

There were no signs of spontaneous coal combustion in 2131(3) and 2121(3) goafs and a coal pillar. First, the 40-d interval between coal seam extraction and the explosion was less than the minimum 54-d autoignition period. Second, CO concentrations in the goaf remained below 20 ppm before March 8 (Fig. 20). In addition, no spontaneous combustion marker gases (C_2H_4, C_2H_2) were detected by gob sensors or at return airway and coal pillar observation points. The post-ignition surge in CO levels likely resulted from hydrocarbon combustion rather than coal self-heating. Subsequent gas combustion initiated localized oxidation/pyrolysis of support-proximate coal bodies, producing transient smoke emissions and pyrolytic tar odors.

(2) Friction sparks between the coal cutter and the rocks

Frictional sparks between picks and hard coal or gangue were considered. However, Fig. 19 shows that on March 8, the shearer was operating at #127–137 supports, approximately 7 m from the explosion site in the goaf and 65 m from the underlying fault zone. During the initial gas explosion, the coal cutter was cutting through soft coal without contacting gangue in the fault zone. Moreover, the separation between the fault zone and the explosion site would have limited flame propagation. Third, video monitoring revealed localized frictional sparks only during the coal cutter contacting the sandy mudstone in the fault. Continuous high-pressure water cooling of the coal cutter and supports effectively suppressed ignition, as shown in Fig. 21. Neither video evidence nor operator reports indicated flame propagation from support fronts to rears or into the goaf area. Thus, friction sparks are unlikely to have been the ignition source.

(3) Electrical ignition of the roof rock fracture

The roof rock samples and mine pressure data were collected on-site, and fracturing experiments were conducted in a methane/air premixed gas condition. The comprehensive analysis concluded that the initial ignition source in the goaf is strongly linked to electrical discharge associated with roof rock failure under loading.

Fig. 22 shows that the initial explosion coincided with periodic roof weighting. The resistance of #35 and #140 supports near the upper corner reached 29.7 and 29.0 MPa, increased by 19.3% and 12.4%, respectively. This indicates continuous stress concentration and pressure on the working face.

At the 2131(3) working face, the immediate roof consists of a 1.8 m thick layer of sandy mudstone, while the main roof is composed of a 4.8 m thick layer of fine sandstone. XRD analysis shows that these strata contain 21.3% and 61.7% quartz, respectively. Notably, the compressive and tensile strengths of the fine sandstone are 3.58 and 2.10 times higher than those of the sandy mudstone, respectively. This enhanced mechanical property correlates with superior discharge capacity during both tensile and compressive failure, as demonstrated in Figs. 8 and 9. The thin immediate roof exhibited low load-bearing capacity and poor free charge accumulation. In contrast, the fine sandstone main roof served as the principal load-bearing stratum. Small-scale fracturing experiments confirmed the capacity for discharge ignition of fine sandstone during failure in methane/air premixed gas, as shown in Fig. 11. When the 4.8 m thick stratum fractures, crack propagation predictably intensifies compared to laboratory specimens. The previous study indicates that the electrical signal from loaded rocks has the scale effect—the larger the scale of the rock stratum, the higher the order of electrical signal magnitude [41]. The piezoelectric and triboelectric effects continuously generate free charges at the crack tips of rock strata, creating high-field-strength zones. The subsequent escape of high-energy electrons into the methane-air mixture then initiates gas ignition through molecular dissociation, as depicted in Fig. 23. While the subsequent explosion is related to the initial explosion, its ignition mechanism remains undetermined. Notably, repeated roof fractures induced by the mining disturbance and explosive shockwave may result in a re-electric ignition. The complexity of such secondary gas explosions warrants further dedicated investigation.

Hydraulic fracturing presents a promising method for weakening these quartz-bearing strata, preventing large-scale fracture concentration [42]. Injecting high-pressure water induces controlled pre-fracturing, mitigating quartz crystal fracture and suppressing rapid crack propagation during periodic roof weighting. Moreover, water reduces rock resistivity, facilitating charge migration and dissipation, which effectively neutralizes piezoelectric potential differences generated during fracturing [43].

To address the risk of gas accumulation, enhanced goaf gas drainage efficiency can be achieved through cooperative drainage systems utilizing high- and low-level roadways coupled with additional extraction pipelines on the return-air side [44]. Concurrently, intensified filling and sealing operations at working faces and upper/lower gob corners are essential to mitigate air leakage [45].

5. Conclusions

To investigate the correlation between gas explosions and rock fracturing during periodic weighting in coal mines, a system was established to simulate rock discharge ignition during loaded fracturing under methane/air premixed gas conditions. The study validated the potential of loaded fracture-induced discharge in roof rocks to ignite methane-air mixtures and elucidated the discharge

(a) Friction spark (b) High-pressure water cooling

Fig. 21. High-pressure water injection to suppress frictional sparks between picks and rocks.

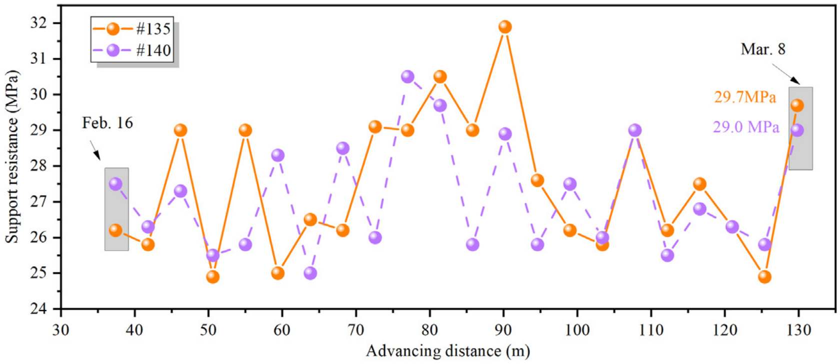

Fig. 22. Change in support resistance near the upper corner.

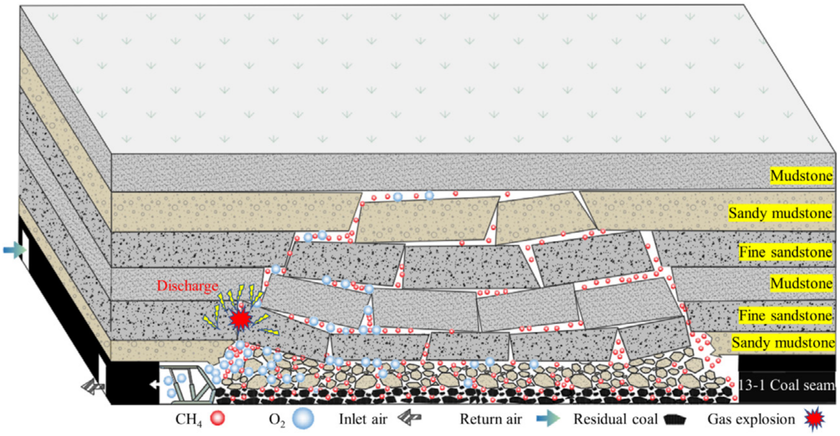

Fig. 23. Gas explosion triggered by the fractured sandstone discharge in the goaf.

ignition mechanism within sandstone fractures. This provides new insights into non-thermal ignition in gas explosions in the goaf. The main conclusions are as follows.

(1) A novel ignition source of gas explosions induced by fracture-induced electrical discharge in roof rocks in goaf, was proposed and verified. Experimental results show that fine and quartz sandstones with quartz content exceeding 61% can ignite methane/air premixed gas at a concentration of 9.5 vol%. The initial flame kernel of the explosion originates at macroscopic fracture surfaces, driven by a discharge spark emanating from fracture tips.

(2) Luminous emission induced by discharge spark is generated via localized gas ionization, a result of free electrons released from fracture tips colliding with ambient gas molecules. The luminescence intensity of rock fracturing serves as an indirect indicator of its discharge ignition ability. Luminescence intensity exhibits linear correlations with surface voltages (R^2=0.9695) and external voltages (R^2=0.9429). This indicates that the accumulation and release of electric charges on the rock surface is the basis for electric ignition. Notably, compression-fractured specimens exhibit more pronounced electrical signal response and luminescence than tension-fractured samples, attributable to enhanced macroscopic crack generation.

(3) A charge generation-discharge-ionization causative chain of electrical ignition resulting from rock fracturing was revealed. The deformation and fracture of sandstones generate a substantial amount of free charge owing to the piezoelectric effect and crack propagation. The accumulation of mobile charges at fracture tips generates intense electric fields, facilitating the emission of high-energy electrons. These emitted electrons subsequently ionize the premixed gas molecules, initiating an electron avalanche that culminates in a gas explosion.

(4) The engineering applicability of rock fracture-induced electrical ignition through field evidence analysis was validated. In the Xieqiao coal mine, traditional thermal ignition sources, such as coal spontaneous combustion and frictional sparks, were excluded owing to the absence of indicator gases and shearer activity. Critically, instantaneous stress release triggered fractures in quartz-rich roof strata during periodic weighting, temporally and spatially coinciding with gas explosions. These findings establish fracture-induced electrical ignition as a novel theoretical framework for explaining such explosion phenomena.

Rock fracture-induced electrical ignition provides a mechanistic explanation for sudden coal mine gas explosions. This insight may also contribute to understanding the origins of fires following earthquakes and to assessing the ignition risk associated with underground hydrogen/natural gas storage in fractured surrounding rock. However, future research should conduct multi-scale loaded rock discharge experiments across the methane concentration of 5%–16%. Furthermore, it is necessary to quantify the ignition energy of discharge spark by rock fracturing using a high-sensitivity optical-electrical monitoring instrumentation in the laboratory and coal mine underground.

Acknowledgements

This work was supported by the National Natural Science Foundation of China (Nos. 52130411, 52174219 and 52174220), the Natural Science Foundation of Jiangsu Province (No. BK20240104), and the Fundamental Research Funds for the Central Universities (No. 2024-11044).

References

[1] Longwell JP, Rubin ES, Wilson J. Coal: Energy for the future. Prog Energy Combust Sci 1995;21(4):269–360.
[2] Chen HY, Liu K, Shi T, Wang LF. Coal consumption and economic growth: A chinese city-level study. Energy Econ 2022;109:105940.
[3] Ray SK, Khan AM, Mohalik NK, Mishra D, Mandal S, Pandey JK. Review of preventive and constructive measures for coal mine explosions: An Indian perspective. Int J Min Sci Technol 2022;32(3):471–85.
[4] Zhu YF, Wang DM, Shao ZL, Xu CH, Zhu XL, Qi XY, Liu FM. A statistical analysis of coalmine fires and explosions in China. Process Saf Environ Prot 2019;121:357–66.
[5] Gao K, Li SN, Han R, Li RZ, Liu ZM, Qi ZP, Liu ZY. Study on the propagation law of gas explosion in the space based on the goaf characteristic of coal mine. Saf Sci 2020;127:104693.
[6] Liang YP, Dai JH, Zou QL, Li L, Luo YJ. Ignition mechanism of gas in goaf induced by the caving and friction of sandstone roof containing pyrite. Process Saf Environ Prot 2019;124:84–96.
[7] Zheng YN, Li SS, Xue S, Jiang BY, Ren B, Zhao Y. Study on the evolution characteristics of coal spontaneous combustion and gas coupling disaster region in goaf. Fuel 2023;349:128505.
[8] Qin GP, Wen ZJ, Wang C, Zhang ZT, Meng DJ. Goaf gas ignition due to hard and thick rock stratum fracture friction effects: A case study. Geotech Geol Eng 2019;37(3):1569–84.
[9] Chen B. Stress-induced trend: The clustering feature of coal mine disasters and earthquakes in China. Int J Coal Sci Technol 2020;7(4):676–92.
[10] Lu Y, Li M, Wang DM, Shi XY, Li H, Zhu YF, Ye Q, Lu JX. Discharge and ignition characteristics from indentation fracture of coal mine roof. Fuel 2021;291:120208.
[11] Freund F. Time-resolved study of charge generation and propagation in igneous rocks. J Geophys Res Solid Earth 2000;105(B5):11001–19.
[12] Li DX, Wang EY, Li ZH, Ju YQ, Wang DM, Wang XY. Experimental investigations of pressure stimulated currents from stressed sandstone used as precursors to rock fracture. Int J Rock Mech Min Sci 2021;145:104841.

[13] Wang W, Pan YS, Zhao HR, Xiao YH, Li XL, Bao XY, Liu Y, Wang JM. Electric charge induction monitoring of deformation and failure behavior of igneous rock: Laboratory test and field applicatio. J Rock Mech Geotech Eng 2025.
[14] Liu HF, Li ZL, He XQ, Wang LB, Song DZ, Tian XH, Qiu LM, Wang WX. Dynamic and static electrical characteristics of micro-surface of rocks by coupled use of atomic force microscope and micro-loading device. Int J Rock Mech Min Sci 2021;148:104977.
[15] Triantis D, Anastasiadis C, Stavrakas I. The correlation of electrical charge with strain on stressed rock samples. Nat Hazards Earth Syst Sci 2008;8(6):1243–8.
[16] Zhang W, Wang DM, Wang CG, Xin HH, Shao ZL, Hou ZH, Zhou WD. Correlation between microstructure-mechanic properties and the pressure-stimulated current response of thermally damaged sandstones: An experimental study. Measurement 2025;253:117540.
[17] Warwick JW, Stoker C, Meyer TR. Radio emission associated with rock fracture: Possible application to the Great Chilean Earthquake of May 22, 1960. J Geophys Res Solid Earth 1982;87(B4):2851–9.
[18] Kawaguchi Y. Charged particle emission and luminescence upon bending fracture of granite. Jpn J Appl Phys 1998;37(6R):3495.
[19] Kadono T, Ogawa K, Shirai K, Arakawa M, Kurosawa K, Okamoto T, Matsui T, Hasegawa S, Suzuki AI, Kobayashi H. Experimental investigation of visible-light and X-ray emissions during rock and mineral fracture: Role of electrons traveling between fracture surfaces. Minerals 2022;12(6):778.
[20] Martelli G, Smith PN, Woodward AJ. Light, radiofrequency emission and ionization effects associated with rock fracture. Geophys J Int 1989;98(2):397–401.
[21] Brady BT, Rowell GA. Laboratory investigation of the electrodynamics of rock fracture. Nature 1986;321(6069):488–92.
[22] Enomoto Y, Hashimoto H. Emission of charged particles from indentation fracture of rocks. Nature 1990;346(6285):641–3.
[23] Cress GO, Brady BT, Rowell GA. Sources of electromagnetic radiation from fracture of rock samples in the laboratory. Geophys Res Lett 1987;14(4):331–4.
[24] Widom A, Swain J, Srivastava YN. Neutron production from the fracture of piezoelectric rocks. J Phys G Nucl Part Phys 2013;40(1):015006.
[25] Takaki S, Ikeya M. A dark discharge model of earthquake lightning. Jpn J Appl Phys 1998;37(9R):5016.
[26] Lockner DA, Johnston MJS, Byerlee JD. A mechanism to explain the generation of earthquake lights. Nature 1983;302(5903):28–33.
[27] Enomoto Y. Coupled interaction of earthquake nucleation with deep Earth gases: A possible mechanism for seismo-electromagnetic phenomena. Geophys J Int 2012;191(3):1210–4.
[28] Enomoto Y, Yamabe T, Sugiura S, Kondo H. Laboratory investigation of coupled electrical interaction of fracturing rock with gases. Earth Planets Space 2021;73(1):90.
[29] Enomoto Y, Komatsubara T, Kiyashu S. Ignition of subterranean methane: Unveiling a new geohazard in Japan following 2024 Noto Peninsula Earthquake. NPJ Nat Hazards 2025;2:31.
[30] Li M, Lu Y, Shi SL, Li H, Tian ZJ, Ye Q, Lu JX. Piezoelectric effect and ignition properties of coal mine roof sandstone deformation and fracture. Fuel 2021;290:120007.
[31] Wang CG, Wang DM, Xin HH, Zhang W, Chen TF, Zhang K. The electrical discharge characteristics and ignition mechanism of coal mine roof fracture under stress. Eng Fract Mech 2025;314:110744.
[32] Zhang YL, Zhou HT, Ma GW, Chen Y. Influence of porosity and mineral composition on the mechanical properties of sandstone under and after cryogenic conditions. Rock Mech Rock Eng 2025;58(8):8799–818.
[33] Bao Q, Fang Q, Zhang YD, Chen L, Yang SG, Li Z. Effects of gas concentration and venting pressure on overpressure transients during vented explosion of methane-air mixtures. Fuel 2016;175:40–8.
[34] Eccles D, Sammonds PR, Clint OC. Laboratory studies of electrical potential during rock failure. Int J Rock Mech Min Sci 2005;42(7–8):933–49.
[35] Bishop JR. Piezoelectric effects in quartz-rich rocks. Tectonophysics 1981;77(3–4):297–321.
[36] Han JH, Huang SL, Zhao W, Wang S, Deng YM. Study on electromagnetic radiation in crack propagation produced by fracture of rocks. Measurement 2019;131:125–31.
[37] Chandra BP, Chandra VK, Jha P, Patel R, Shende SK, Thaker S, Baghel RN. Fracto-mechanoluminescence and mechanics of fracture of solids. J Lumin 2012;132(8):2012–22.
[38] Popov NA. Fast gas heating in a nitrogen-oxygen discharge plasma: I. Kinetic mechanism. J Phys D Appl Phys 2011;44(28):285201.
[39] St-Laurent F, Derr JS, Freund FT. Earthquake lights and the stress-activation of positive hole charge carriers in rocks. Phys Chem Earth Parts A/B/C 2006;31(4–9):305–12.
[40] Lintin DR, Wooding ER. Investigation of the ignition of a gas by an electric spark. Br J Appl Phys 1959;10(4):159.
[41] Li DX, Wang EY, Feng XJ, Wang DM, Zhang X, Ju YQ. Weak current induced by coal deformation and fracture and its response to mine seismicity in a deep underground coal mine. Eng Geol 2023;315:107018.
[42] Huang BX, Wang YZ, Cao SG. Cavability control by hydraulic fracturing for top coal caving in hard thick coal seams. Int J Rock Mech Min Sci 2015;74:45–57.
[43] Li HR, Qiao YF, Shen RX, He MC. Electromagnetic radiation signal monitoring and multi-fractal analysis during uniaxial compression of water-bearing sandstone. Measurement 2022;196:111245.
[44] Zhang H, Cheng YP, Deng CB, Jiang JY, Zhang L. Stress-unloading and gas migration improvement mechanism in the soft and hard interbedded coal seam using directional hydraulic flushing technology. Int J Min Sci Technol 2023;33(9):1165–79.
[45] Zhou M, Li S, Zheng Z, Liu R, Chen M, Ma C. Theoretical and experimental study on the rheological properties of WIS grout and the dispersion and sealing mechanism. Int J Min Sci Technol 2022;32(4):669–84.